Journal of Computational Electronics (2021) 20:1676–1684
https://doi.org/10.1007/s10825-021-01751-2

A unified compact model for electrostatics of III–V GAA transistors with different geometries

Mohit D. Ganeriwala[1] · Francisco G. Ruiz[2] · Enrique G. Marin[2] · Nihar R. Mohapatra[1]

Received: 1 December 2020 / Accepted: 20 July 2021 / Published online: 7 August 2021

Abstract
In this work, a physics-based unified compact model for III-V GAA FET electrostatics is proposed. The model considers arbitrary cross-sectional geometry of GAA FETs viz. rectangular, circular and elliptical. A comprehensive model for cuboid GAA FETs is developed first using the constant charge density approximation. The model is then combined with the earlier developed model for cylindrical GAA FETs to have a unified representation. The efficacy of the model is validated by comparing it with simulation data from a 2D coupled Poisson-Schrödinger solver. The proposed model is found to be, (a) accurate for GAA FETs with different geometries, dimensions and channel materials and (b) computationally efficient.

Keywords Gate all around FET · Nanowire · III–V · Compact model · Charge · Surface potential · Capacitance · Circuit simulation

1 Introduction

The Gate-All-Around (GAA) transistors (nanowire and nanosheet FETs) are being actively considered for Sub-5 nm CMOS technology nodes because of their superior gate electrostatics [1–3]. Along with the gate all around geometry, the GAA FETs with III-V channel materials have shown potential for high speed and low power ULSI circuits [4–6]. Several research groups have successfully demonstrated large scale fabrication of III-V GAA FETs in last few years [7–10]. Note that the GAA FETs are realized in different geometries (cylindrical (Fig. 1a) and cuboid (Fig. 1c)). Further, considering the process variations in Sub-10 nm CMOS technologies, the cylindrical GAA FETs can also have an elliptical cross-section instead of the desired circular one (Fig. 1b). Because of these different cross-sectional geometries, the modeling of GAA FET electrostatics is complicated. It is therefore necessary to have a unified model which could capture the electrical response of GAA FETs with different geometries and dimensions. The unified model will reduce the effort during the model implementation at the circuit level.

Most of the industry standard compact models for GAA FETs are semi-classical in nature. These models are not suitable for simulating the III-V channel GAA FETs. The reason behind this is high quantum confinement in the GAA FETs and lower DOS of III-V materials [11–14]. The significant separation between energy levels and the sub-band formation results in a quasi 1D system. Also, due to lower DOS, the Fermi level penetrates into the conduction band rendering the Boltzmann approximation ineffective [15]. This necessitates solution of the coupled Poisson-Schrödinger (PS) equation with full Fermi-Dirac statistics, to model the III-V GAA FETs [16]. However, because of the substantial computational burden of the coupled PS equation, it is not suitable for circuit simulators. The recent revision to BSIM model has included the quantum effects on top of the BSIM-CMG semi-classical core. However, it uses mostly empirical equations and a large number of additional fitting parameters [17]. Several physics-based compact models treating III-V channel transistor electrostatics using energy perturbation approach have also been reported [11, 12, 14, 18]. In particular, these models need sub-band wave-function to calculate the charge density. However, it is not always possible to calculate the wave-function (which is also dependent on FET geometry) analytically. Our research group have recently

✉ Mohit D. Ganeriwala
ganeriwala.mohit@gmail.com

[1] Department of Electrical Engineering, Indian Institute of Technology Gandhinagar, Gandhinagar, Gujarat 382355, India

[2] Department of Electronics, University of Granada, Granada, Spain

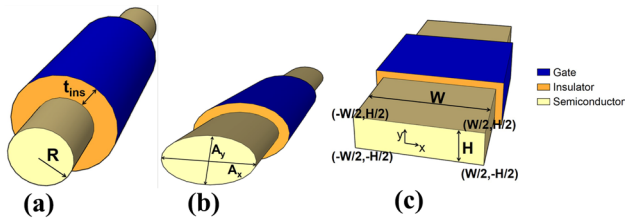

Fig. 1 Cross-sectional view of the GAA FETs with, **a** Circular cross-section, **b** Elliptical cross-section and **c** Rectangular cross-section. Cartesian coordinate system is considered for modeling of the cuboid GAA FETs with rectangular cross-section, while cylindrical coordinate system is considered for cylindrical GAA FETs with circular and elliptical cross-sections

reported a constant charge density approximation (CCDA) [13]. The CCDA eliminates the need for prior knowledge of exact wave-function. Using the CCDA, the electrostatics of cylindrical GAA FETs with a perfectly circular cross-section had been modeled and reported in [13]. However, there is a need to develop a similar model for cuboid GAA FETs (rectangular cross-section) and cylindrical GAA FETs (elliptical cross-section). Note that the modeling of a cuboid GAA FET is complicated since the insulator-semiconductor interface is non-isopotential and hence the conventional MOS transistor equations could not be directly applied.

Several attempts had been made in the past to model electrostatics of cuboid GAA FETs. In [12], a model for cuboid III-V GAA FET with square cross-section was presented. The model used energy values and perturbation terms directly from [11], which was calculated for a 1D potential well. This is inaccurate for a 2D confined square geometry. Also, the sub-band degeneracy inherent in the symmetry of a 2D potential well was neglected and the non-isopotential nature of the insulator-semiconductor interface was also ignored. Similar work in [14], proposed a unified model applicable for cuboid and cylindrical (with a circular cross-section) GAA FETs. The model incorporated the geometry change by modifying only the insulator capacitance, which obliterates the quantum physics in these confined structures. Further, the energy and the perturbation terms were taken directly from [11] and thus has all inaccuracies of the model presented in [12]. A model for cuboid GAA FET (rectangular cross-section) proposed in [19], addressed some of these inaccuracies by considering the non-isopotential insulator-semiconductor interface. However, a pseudo-empirical potential function inside the semiconductor channel was assumed, which complicated the model equations. In [19], the perturbation terms were also derived for an infinite potential well structure, which is inaccurate.

In this work, we have used the CCDA, considered the non-iso-potential insulator semiconductor interface and at the same time ensured that the equations have the conventional form. The model for GAA FETs with circular and a rectangular cross-sections are then combined to present a unified model. The CCDA is highly beneficial in this scenario as the most significant part of geometry dependence, which comes through the wave-function, is resolved. The model proposed in this work is mathematically simple, can include higher energy sub-bands and is computationally efficient for circuit simulations. It is also shown that the structural variations in the cylindrical GAA FETs will not affect the transistor electrostatics significantly. Therefore, by considering the structural variations as a perturbation to the symmetric structure, the model is extended for an elliptical cross-section GAA FETs by tuning the sub-band energy levels. The proposed model therefore captures the electrostatics of III-V GAA FETs with different cross-sectional geometries and dimensions.

The proposed model is further extended to integrate the conduction band non-parabolicity and the change in the carrier effective mass with channel thickness, crucial for III-V materials. The model is then verified with the simulation data from 2D PS solver, for GAA FETs with different gate geometries, dimensions and channel materials. It is shown that the model is valid for rectangular, circular and elliptical cross-section GAA FETs. It is also shown that the model could be directly used for nanosheet FETs and multi-bridge channel FETs (MBCFETs).

The paper is organized as follow: In section 2, the proposed model is described. The model for rectangular cross-section GAA FETs is introduced first. This model is then combined with the one for circular cross-section to implement a unified model. The unified model is validated in section 3 with the data from 2D PS solver. The applicability of the proposed model for elliptical cross-section is also discussed in this section followed by conclusion in Section 4.

2 Model

2.1 Electrostatic model for cuboid GAA FETs

Figure 1c shows the cross-section of a generic III-V GAA FET with rectangular cross section. Here, H and W are height and width of the FET, respectively, t_{ins} is the gate insulator thickness. The cartesian coordinates, as shown in Fig. 1c are used for the model derivation.

The potential balance equation across H and W of the GAA FET can be written as,

$$V_G = \Phi'_{ms} + V_{ins,x}(y) + \Phi\left(-\frac{W}{2}, y\right) \tag{1}$$

$$V_G = \Phi'_{ms} + V_{ins,y}(x) + \Phi\left(x, -\frac{H}{2}\right) \tag{2}$$

Here, V_G is the gate voltage, $\Phi'_{ms} = \Phi_m - \chi$, Φ_m is the metal work function, χ is the electron affinity of the

semiconductor, $V_{\mathrm{ins,x}}(y)$ and $V_{\mathrm{ins,y}}(x)$ are potential drops across the gate insulator in x and y directions, respectively. $\boldsymbol{\Phi}(x, y)$ is the potential inside the semiconductor channel. The $\boldsymbol{\Phi}(x, y)$ can be written as $\boldsymbol{\Phi}(x, y) = -(E_{\mathrm{c}}(x, y) - E_{\mathrm{f}})/q$, where $E_{\mathrm{c}}(x, y)$ is bottom of the conduction band, E_{f} is the Fermi level and q is the electronic charge. $E_{\mathrm{f}} = 0$ is assumed as the reference for energies unless otherwise specified.

The potential at the insulator-semiconductor interface ($\boldsymbol{\Phi}(x, -H/2)$) and ($\boldsymbol{\Phi}(-W/2, y)$) is not constant along W or H. Therefore, a single value of the surface potential or insulator voltage drop cannot be directly defined. However, if we take the average across W and H, an effective surface potential ($\boldsymbol{\Phi}_{\mathrm{s,eff}}$) and effective insulator drop ($V_{\mathrm{ins,eff}}$) can be defined as follows.

$$\int_{-\frac{H}{2}}^{\frac{H}{2}} V_{\mathrm{G}}\mathrm{d}y = \int_{-\frac{H}{2}}^{\frac{H}{2}} \boldsymbol{\Phi}_{\mathrm{ms}}\mathrm{d}y + \int_{-\frac{H}{2}}^{\frac{H}{2}} V_{\mathrm{ins,x}}(y)\mathrm{d}y + \int_{-\frac{H}{2}}^{\frac{H}{2}} \boldsymbol{\Phi}\left(-\frac{W}{2}, y\right)\mathrm{d}y \tag{3}$$

By defining, $1/H \int_{-H/2}^{H/2} V_{\mathrm{ins,x}}(y)\mathrm{d}y = V_{\mathrm{ins,eff}}$ and $1/H \int_{-H/2}^{H/2} \boldsymbol{\Phi}(-W/2, y)\mathrm{d}y = \boldsymbol{\Phi}_{\mathrm{s,eff}}$, we can write,

$$V_{\mathrm{G}} = \boldsymbol{\Phi}'_{\mathrm{ms}} + V_{\mathrm{ins,eff}} + \boldsymbol{\Phi}_{\mathrm{s,eff}} \tag{4}$$

Same can be written by taking an average over W in (2). Equation (4) is a more conventional form of the potential balance equation. It also leads to the observation that,

$$\frac{1}{H}\int_{-\frac{H}{2}}^{\frac{H}{2}} V_{\mathrm{ins,x}}(y)\mathrm{d}y = \frac{1}{W}\int_{-\frac{W}{2}}^{\frac{W}{2}} V_{\mathrm{ins,y}}(x)\mathrm{d}x \tag{5}$$

$$\frac{1}{H}\int_{-\frac{H}{2}}^{\frac{H}{2}} \boldsymbol{\Phi}\left(-\frac{W}{2}, y\right)\mathrm{d}y = \frac{1}{W}\int_{-\frac{W}{2}}^{\frac{W}{2}} \boldsymbol{\Phi}\left(x, -\frac{H}{2}\right)\mathrm{d}x \tag{6}$$

The correctness of both (5) and (6) is verified using data from the PS solver.

To find $\boldsymbol{\Phi}(x, y)$ inside the channel, the following 2D Poisson equation is solved.

$$\frac{\partial^2\boldsymbol{\Phi}(x, y)}{\partial x^2} + \frac{\partial^2\boldsymbol{\Phi}(x, y)}{\partial y^2} = q\frac{n(x, y)}{\varepsilon_{\mathrm{s}}} \tag{7}$$

Here, ε_{s} is the permittivity of channel material and $n(x, y)$ is the volume charge density, given by,

$$n(x, y) = \sum_{i,j} g_{\mathrm{v}}\sqrt{\frac{2m^*k_{\mathrm{B}}T}{\pi\hbar^2}}F_{-\frac{1}{2}}\left(-\frac{E_{i,j} - q\boldsymbol{\Phi}_{\mathrm{c}}}{k_{\mathrm{B}}T}\right)|\boldsymbol{\Psi}_{i,j}(x, y)|^2 \tag{8}$$

In (8), g_{v} is the valley degeneracy ($g_{\mathrm{v}} = 1$ for the Γ valley), k_{B} is the Boltzmann constant, m^* is the effective mass, T is the temperature, $\hbar$ is the reduced Plank's constant, $F_{-1/2}$ is the Fermi Dirac integral of order $-1/2$, $E_{i,j}$ is the sub-band energy level (with reference to $E_{\mathrm{c}}(0, 0)$) and $\boldsymbol{\Phi}_{\mathrm{c}}$ is the center potential (at (x,y) = (0,0)) and $\boldsymbol{\Psi}_{i,j}(x, y)$ is the sub-band wave function. To calculate both $E_{i,j}$ and $\boldsymbol{\Psi}_{i,j}(x, y)$, the Schrödinger equation needs to be solved for each $\mathrm{V_G}$. This couples the Poisson and the Schrödinger equation thus increasing the computational cost of the model. However, using CCDA, the $|\boldsymbol{\Psi}_{i,j}(x, y)|^2$ can be approximated as $|\boldsymbol{\Psi}_{i,j}(x, y)|^2 = 1/WH$ (refer Appendix 1). The CCDA relies on the fact that from a compact model perspective, the $n(x, y)$ profile can be approximated if the terminal charges, i.e., the charge per unit length ($\mathrm{Q_s}$) is known with considerable accuracy. Therefore, in the CCDA, the n(x,y) is assumed to be constant inside the channel such that $\mathrm{Q_s}$ is accurate i.e., $-qn(x, y) = \frac{Q_{\mathrm{s}}}{WH}$. Here, the $\mathrm{Q_s}$ is given by,

$$Q_{\mathrm{s}} = -q\sum_{i,j} g_{\mathrm{v}}\sqrt{\frac{2m^*k_{\mathrm{B}}T}{\pi\hbar^2}}F_{-\frac{1}{2}}\left(-\frac{E_{i,j} - q\boldsymbol{\Phi}_{\mathrm{c}}}{k_{\mathrm{B}}T}\right) \tag{9}$$

Since, the source term $qn(x, y)/\varepsilon_{\mathrm{s}}$ in (7) is approximated with a constant profile inside the channel, it is safe to assume $\boldsymbol{\Phi}(x, y)$ to be parabolic. Therefore,

$$\boldsymbol{\Phi}(x, y) = Ax^2 + By^2 + Cx + Dy + E \tag{10}$$

Here, A, B, C, D and E are arbitrary constants to be determined by using the boundary conditions. Substituting (10) in (7) and using appropriate boundary conditions, $\boldsymbol{\Phi}(x, y)$ can be derived analytically as a function of $\mathrm{Q_s}$ as (details in Appendix 2),

$$\boldsymbol{\Phi}(x, y) = \boldsymbol{\Phi}_{\mathrm{c}} - \frac{Q_{\mathrm{s}}}{2\varepsilon_{\mathrm{s}}\left(W^2 + H^2\right)}\left[\frac{H}{W}x^2 + \frac{W}{H}y^2\right] \tag{11}$$

Applying the definition of $\boldsymbol{\Phi}_{\mathrm{s,eff}}$, a relation between $\boldsymbol{\Phi}_{\mathrm{s,eff}}$ and $\boldsymbol{\Phi}_{\mathrm{c}}$ can be established as below.

$$\boldsymbol{\Phi}_{\mathrm{s,eff}} = \boldsymbol{\Phi}_{\mathrm{c}} - \frac{Q_{\mathrm{s}}WH}{6\varepsilon_{\mathrm{s}}\left(W^2 + H^2\right)} \tag{12}$$

Now, using the Gauss law one can also write,

$$Q_{\mathrm{s}} = 2\varepsilon_{\mathrm{s}}\left[\int_{-\frac{H}{2}}^{\frac{H}{2}} F_{\mathrm{x,s}}\mathrm{d}y + \int_{-\frac{W}{2}}^{\frac{W}{2}} F_{\mathrm{y,s}}\mathrm{d}x\right] \tag{13}$$

Here, $F_{\mathrm{x,s}}$ and $F_{\mathrm{y,s}}$ are the surface electric fields calculated as $\partial\boldsymbol{\Phi}(x, y)/\partial x|_{x=-W/2}$ and $\partial\boldsymbol{\Phi}(x, y)/\partial y|_{y=-H/2}$, respectively. Substituting the dielectric boundary condition $C_{\mathrm{ins}}V_{\mathrm{ins,x}} = \varepsilon_{\mathrm{s}}F_{\mathrm{x,s}}$ in (13) and using (5), $\mathrm{V_{ins,eff}}$ can be expressed as a function of $\mathrm{Q_s}$ as,

$$V_{\mathrm{ins,eff}} = -\frac{Q_s}{2C_{\mathrm{ins}}(W + H)} \tag{14}$$

Using (14) and (12), (4) can be re-written as,

$$Q_s = -2C_{ins,eff}(V_G - \Phi'_{ms} - \Phi_c) \tag{15}$$

In (15), $C_{ins,eff}$ is the effective insulator capacitance and it captures the effect of charge centroid. It is similar to the conventional method of introducing the oxide thickness correction based on the charge centroid, which is given by,

$$C_{ins,eff} = \frac{C_{ins}(W+H)}{1 + \frac{C_{ins}(W+H)WH}{3\varepsilon_s(W^2+H^2)}} \tag{16}$$

Finally, the sub-band energies $E_{i,j}$ can be written as,

$$E_{i,j} = Eg_{i,j} + \Delta Ee_{i,j} \tag{17}$$

Here, $Eg_{i,j}$ is the sub-band energy considering geometrical confinement and $\Delta Ee_{i,j}$ is the perturbation term added to model the electrical confinement due to band bending. To calculate the $Eg_{i,j}$, the following Schrödinger equation for a constant potential is solved,

$$-\frac{\hbar^2}{2m^*}\left[\frac{\partial^2\Psi_{i,j}}{\partial x^2} + \frac{\partial^2\Psi_{i,j}}{\partial y^2}\right] = Eg_{i,j}\Psi_{i,j}(x,y) \tag{18}$$

Since $Eg_{i,j}$ considers only the geometrical confinement, the potential inside the channel is Φ_c and the same is used as a reference to solve the Schrödinger equation. The separation of variable method can be used to solve (18). The Schrödinger equation, therefore, can be split into two 1D equations and the $Eg_{i,j}$ can be written as a sum of Ex_i and Ey_j. Here, Ex_i and Ey_j are the energy level of a finite potential well equivalently in x- and y-directions, respectively, and can be calculated as in [11]. The $\Delta Ee_{i,j}$ can be calculated as,

$$\Delta Ee_{i,j} = < \Psi^*_{i,j}|\widetilde{\Phi}|\Psi_{i,j} > \tag{19}$$

In (19), the perturbing potential is given by $\widetilde{\Phi}(x,y) = \Phi(x,y) - \Phi_c$. Here, Φ_c is used as a reference to calculate $Eg_{i,j}$ as specified above. Using the CCDA, (19) can be calculated analytically as (details in Appendix 3),

$$\Delta Ee_{i,j} = \frac{qQ_sWH}{12\varepsilon_s\left(W^2+H^2\right)} \tag{20}$$

Note that the perturbation term in (20) is scalable to any number of sub-bands without increasing the mathematical complexity. Using (15) for Q_s in (20) and substituting $\Delta Ee_{i,j}$ in (9),

$$Q_s = -C_q\sum_{i,j}F_{-\frac{1}{2}}\left(\frac{q\Phi_c(1-C_x) - Eg_{i,j} + qC_x(V_G - \Phi'_{ms})}{k_BT}\right) \tag{21}$$

Here, $C_q = qg_v\sqrt{2m^*k_BT/\pi\hbar^2}$ and $C_x = 2C_{ins,eff}WH/12\varepsilon_s(W^2+H^2)$. The equations (21) and (15) can be equated for Φ_c which can then be used in (15) and (12) to get Q_s and $\Phi_{s,eff}$, respectively.

$$Q_s = -\left\{GEO(2C_{ins,eff}) + (1-GEO)C'_{ins,eff}\right\}\left[V_G - \Phi'_{ms} - \Phi_c\right] \tag{22}$$

$$Q_s = -\left[GEO\left\{C_q\sum_{i,j}F_{-\frac{1}{2}}\left(\frac{q\Phi_c(1-C_x) - Eg_{i,j} + qC_x(V_G - \Phi'_{ms})}{k_BT}\right)\right\} + (1-GEO)\left\{C_q\sum_{j}F_{-\frac{1}{2}}\left(\frac{q\Phi_c(1-C'_x) - E'g_j + qC'_x(V_G - \Phi'_{ms})}{k_BT}\right)\right\}\right] \tag{23}$$

2.2 The unified model

The equations (15) and (21) are the final model equations for a cuboid GAA FET. These equations are similar to the one derived for a cylindrical GAA FET with circular cross-section ((9) and (13) in [13]). Therefore, an unified model can be easily constructed by defining a geometry parameter GEO. Equation (22) and (23) describes the unified model. In these equations, GEO = 1 for cuboid and GEO = 0 for cylindrical GAA FETs. The unprimed terms are for the cuboid GAA FETs and carries the same definition as in sec II (A), whereas the primed terms are for cylindrical GAA FETs and are defined as,

$$C'_{ins,eff} = C'_{ins}/(1 + C'_{ins}/4\pi\varepsilon_s),$$
$$C'_x = C'_{ins,eff}/8\pi\varepsilon_s,$$
$$C'_{ins} = 2\pi\varepsilon_{ins}/ln(1 + t_{ins}/R_0)$$

Here, t_{ins} is the insulator thickness and R_0 is the semiconductor radius (refer Fig. 1a).

It is important to note that changing the insulator capacitance is not sufficient to capture geometry variation of the GAA FETs. The energy levels and the potential profile also vary with the geometry and cross-section. The proposed model considered explicitly the physics embedded in the GAA FET geometries and have presented a unified model.

3 Results and discussions

In this section, the proposed model is compared and validated with simulation data from 2D self-consistent Poisson-Schrödinger (PS) solver [20, 21]. The results are shown for GAA FETs with different geometries, dimensions and channel materials. 1.5 nm Al_2O_3 is used as gate insulator for all the simulations. The material parameters are taken from [22] and [23]. The expression for $F_{-1/2}$, as proposed in [24], is used to solve (23). This eliminates the need to uses any tabular function.

Figure 2a, b shows the normalized $\Phi_{s,eff}$ and Φ_c for $In_{0.53}Ga_{0.47}As$ GAA FET with H = 5 nm and different W (the simulated and the modeled data are shown with symbols and solid lines, respectively). For clear visualization, the values of $\Phi_{s,eff}$ and Φ_c for $In_{0.53}Ga_{0.47}As$ are normalised with W. As shown, the model agrees well with the PS solver data. Unlike the silicon channel transistors, $\Phi_{s,eff}$ in III-V channel GAA FETs does not saturate at higher V_G. This confirms the lower DOS in III-V channel materials. Figure 2c, d compares modeled $\Phi_{s,eff}$ and Φ_c for InAs, $In_{0.53}Ga_{0.47}As$ and GaAs GAA FETs (W = H = 5 nm) with the PS solver data. As shown, the model is valid for different III-V channel materials. It is worthwhile to note that the averaging takes care of any error introduced by the assumed potential. Therefore, the calculated $\Phi_{s,eff}$ from the model shows an excellent match with the PS solver data.

Figure 3a–c compares the modeled Q_s with the PS solver data for GAA FETs (rectangular cross-section) with different dimensions and channel materials. Figure. 4a, b compares modeled C_{gg} of the same samples with the PS solver

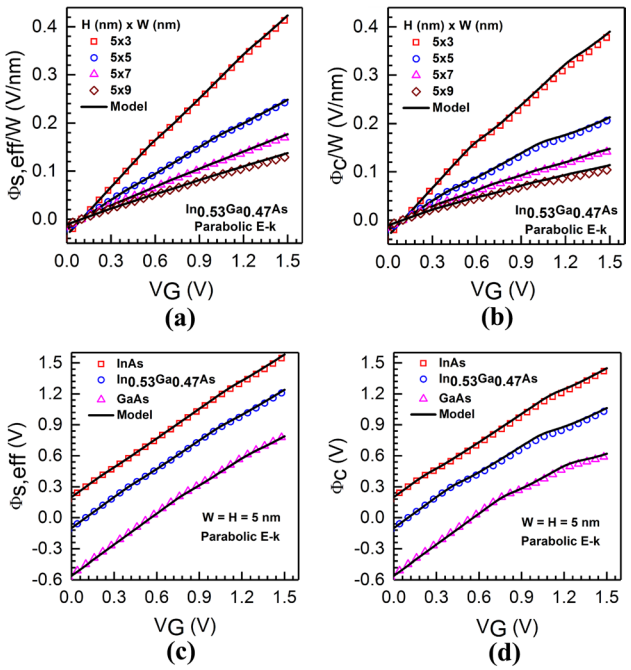

Fig. 2 **a** Effective surface potential, $\Phi_{s,eff}$ and **b** Center potential, Φ_c for $In_{0.53}Ga_{0.47}As$ GAA FETs with H = 5 nm and varied W. **c** $\Phi_{s,eff}$ and **d** Φ_c for InAs, $In_{0.53}Ga_{0.47}As$ and GaAs GAA FETs with W = H = 5 nm. The model matches very well with the simulation data from 2D PS solver. All data are for cuboid GAA FETs with rectangular cross-section (GEO = 1)

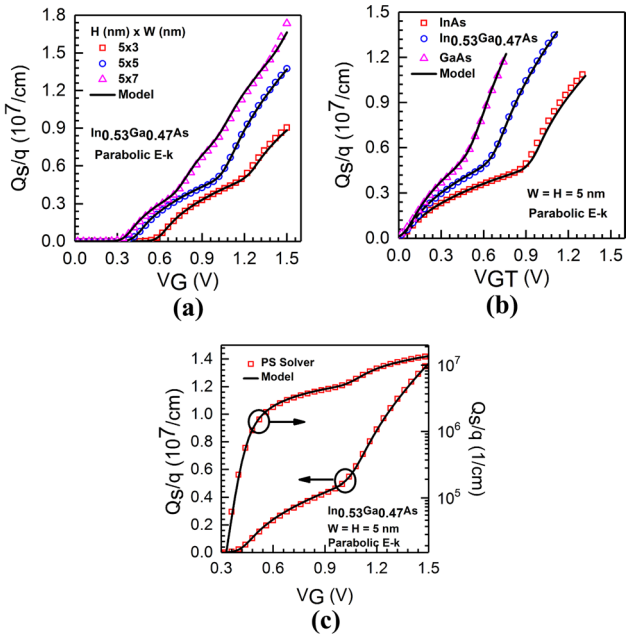

Fig. 3 Charge density Q_s/q as a function of, **a** V_G for $In_{0.53}Ga_{0.47}As$ GAA FETs with H = 5 nm and varied W, **b** Gate overdrive voltage ($V_{GT} = V_G - V_T$) for W = H = 5 nm InAs, $In_{0.53}Ga_{0.47}As$ and GaAs GAA FETs and **c** V_G for W = H = 5 nm $In_{0.53}Ga_{0.47}As$ GAA FET in log and linear scale. The model shows a good agreement with the PS solver data for all applied bias voltages. All data are for the cuboid GAA FET with rectangular cross-section (GEO = 1)

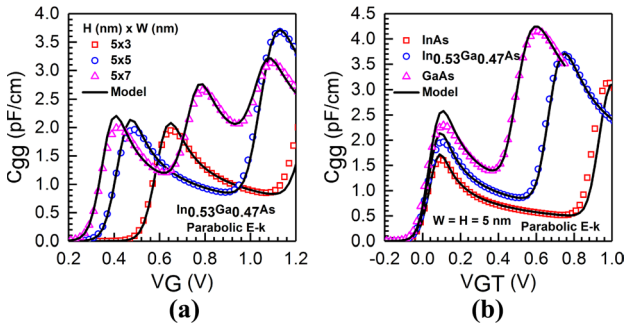

Fig. 4 Gate capacitance C_{gg} as a function of, **a** V_G for $In_{0.53}Ga_{0.47}As$ GAA FETs with H = 5 nm and different W, **b** Gate overdrive voltage ($V_{GT} = V_G - V_T$) for W = H = 5 nm InAs, $In_{0.53}Ga_{0.47}As$ and GaAs GAA FETs. The model could follow the simulated C_{gg} very well. All the data here are for GAA FET with a rectangular cross-section (GEO = 1)

data. As expected, the model matches very well with the PS solver data for a wide range of V_G. As shown, the C_{gg} of rectangular cross-section GAA FETs have humps because of the quasi 1D DOS. Here, each hump corresponds to a particular sub-band and the negative slope of the C_{gg} is due to the inverse square root dependence of 1D DOS on energy.

Figures 2, 3 and 4 validated the accuracy of proposed electrostatic model for cuboid GAA FETs with different channel materials, cross-sections and dimensions. This model could also be used for nano-sheet FETs (i.e., structures with larger W to H ratio) as demonstrated in Fig. 5a. The capability of the model to accurately reproduces characteristics of GAA FETs with different cross-sections is assessed in Fig. 5b. By changing the GEO parameter, the model is able to fit C_{gg} for cylindrical and cuboid geometries. Note, since the electrostatic model for the cylindrical geometry is discussed in detail elsewhere [13], it is not reproduced here.

Further, the fabrication of a cylindrical GAA FET with circular symmetric cross-section is often not possible, due to variations during fabrication. In this work, it is assumed that such variations could lead to an elongated circle or elliptical cross-section GAA FET. Such a cross-section can be characterized by length of its semi-major/minor axis A_x and A_y (Fig. 1b) and amount of variations can be classified based on the difference between A_x and A_y. Assuming that the variations are small, the elliptical cross-section has a minor impact on the electrical characteristic of the GAA FETs. For example, Fig. 6a compares C_{gg} of an $In_{0.53}Ga_{0.47}As$ GAA FET with circular (D = 10 nm) and elliptical (A_y = 10 nm and A_x = 8 nm) cross-section. As shown, the C_{gg} vs. V_G trend is almost similar with a shift in the characteristics. This shift is attributed to the change in sub-band energy levels because of the structural change. Figure 6b shows

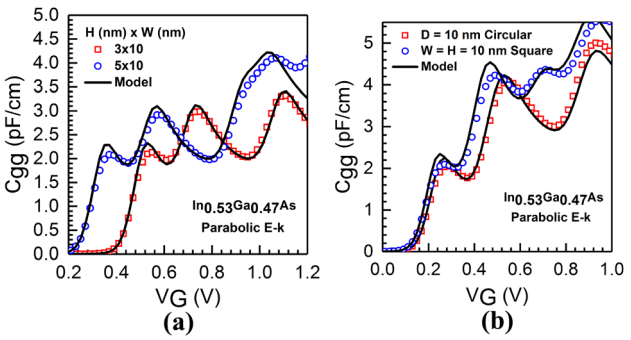

Fig. 5 C_{gg} as a function of V_G for, **a** $In_{0.53}Ga_{0.47}As$ GAA FETs with smaller H and larger W, resembling the nanosheet FETs and **b** for $In_{0.53}Ga_{0.47}As$ cuboid GAA FETs with rectangular cross-section of W = H = 10 nm and Cylindrical GAA FETs with circular coss-section of D = 10 nm. Here, the unified model equations with GEO = 1 is used for the cuboid GAA FET and GEO = 0 for the cylindrical GAA FET. The model matches very well for both the geometries

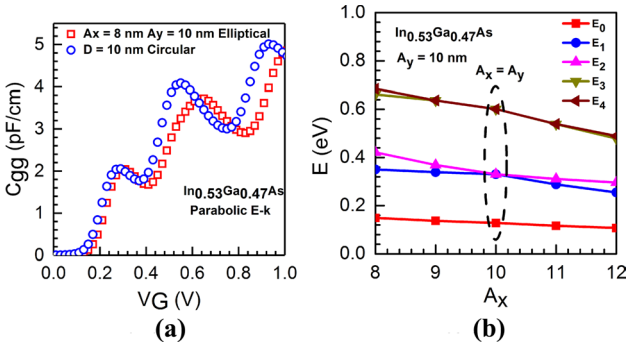

Fig. 6 **a** Comparison of the simulated C_{gg} of the GAA FET with D = 10 nm circular cross-section and A_y = 10 nm and A_x = 8 nm elliptical cross-section. C_{gg} shows similar behavior with a shift in the characteristics and **b** Sub-band energy levels for elliptical GAA FETs with A_y = 10 nm as a function of A_x. The sub-band energy level shows minimal change with A_x with reference to value for $A_x = A_y$

the sub-band energy level for cylindrical GAA FETs with A_y = 10 nm and different A_x. The sub-band energies for the circular symmetric cross-section ($A_x = A_y$) are highlighted in the same figure. As shown, there is a minimal change in the energy level with A_x when compared to their value for symmetric cross-section. Note that it is analytically challenging to exactly calculate the energy levels for the elliptical geometry due to the complexity involved in solving the Schrödinger equation. However, since the variation is not large, the energy level can be tuned to get the desired characteristics. Therefore, in our model, the sub-band energy level $E'g_j$ is modified to $E'g_j + \delta$. The δ is tuned to match the characteristic of the cylindrical GAA FETs with elliptical cross-section. Figure 7 plots the modeled and the simulated Q_s and C_{gg} for $In_{0.53}Ga_{0.47}As$ elliptical GAA FET with A_y = 10 nm and different A_x. The model matches the PS solver data extremely well for the elliptical GAA FETs. Therefore, the proposed unified model could be efficiently applied to the cylindrical geometry (elliptical cross-section) without affecting the model complexity. For elliptical cross-section FETs,

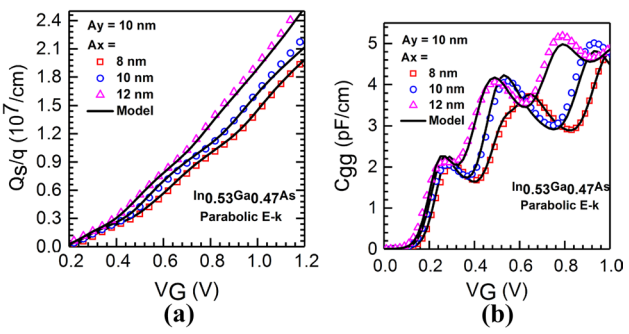

Fig. 7 **a** Semiconductor charge density, Q_s/q as a function of V_G and **b** Gate capacitance, C_{gg} as a function of V_G for $In_{0.53}Ga_{0.47}As$ GAA FETs (elliptical cross-section) with A_y = 10 nm and different A_x

only the geometrical sub-band energies are adjusted, which are bias independent. Therefore, δ is a process dependent model parameter.

It is worthwhile to note that the model derived in this work is based on the assumption of a parabolic Energy-wavevector (E-k) dispersion relation. However, for the III-V materials, the conduction band E-k dispersion relation is highly non-parabolic. Also, the lower DOS causes the Fermi level to penetrate well above the conduction band edge [25]. Due, to which, the parabolic dispersion approximation can introduce relevant inaccuracies into the model [25]. Incidentally, the assumptions used in the model derivation, which led to standard form of the model equation and later to unification of the model, also presents a way to include the band non-parabolicity into the model. One of our previous works has presented an approximate E-k relation to include the conduction band non-parabolicity efficiently into the model, while preserving both the accuracy and simplicity of the compact model [25]. The model in [25] was presented for a cylindrical GAA FETs with circular cross-section. However, the dispersion relation presented there was independent of the channel geometry and hence can directly be applied to the unified model (derived in this work), to include the band non-parabolicity in the cuboid GAA FETs as well. Figure 8a shows the C_{gg} data for an $In_{0.53}Ga_{0.47}As$ channel cuboid GAA FET with different dimensions considering band non-parabolicity. The modified model after considering the band non-parabolicity agrees very well with the PS solver data. A dotted line in Fig. 8a shows the data with the parabolic dispersion approximation for comparison. It can be seen that with the parabolic approximation the C_{gg} values are underestimated. Therefore, it is important to include the band non-parabolicity into the model. And the proposed model efficiently addresses that.

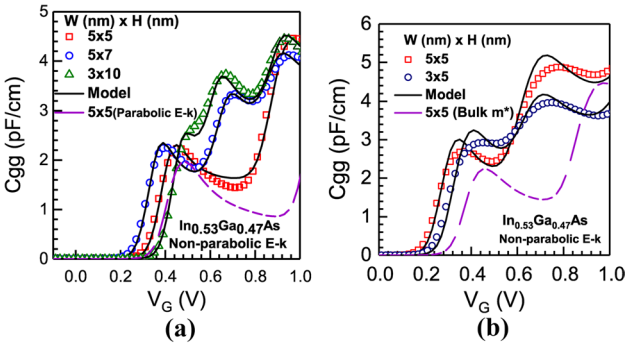

Fig. 8 Gate capacitance, C_{gg} as a function of V_G for $In_{0.53}Ga_{0.47}As$ cuboid GAA FETs with **a** non-parabolic E-k dispersion relation for different channel dimensions. Symbols and the solid line represent the PS solver data and the model, respectively. The dotted line shows the PS solver data with parabolic E-k approximation for comparison. and **b** considering the change in effective mass (m*) with channel thickness. Here, the dispersion relation is non-parabolic. The dotted line represents the PS solver data with the bulk value of the m* for comparison

It is also, important to note that the effective mass (m*) changes with the semiconductor channel thickness. It is crucial especially in lower channel dimension and highly confined devices such as the ones considered in this work. Since, the m* is an input parameter of the model, the change in m* can seamlessly be integrated into the model. Figure 8b shows the model and the PS solver C_{gg} data for an $In_{0.53}Ga_{0.47}As$ channel cuboid GAA FET with different dimensions. Here, the model is shown to capture the m* variation well. The dotted line in Fig. 8b shows the C_{gg} for the same device with the bulk m* value. It can be seen that the C_{gg} changes after considering the change in the m* with confinement, where the m* increases compare to its bulk value. Note that the value of the m* changes is incorporated into the model using the empirical relation proposed by [26] together with the non-parabolic dispersion relation.

4 Conclusion

To summarize, a unified compact electrostatic model for III-V GAA FETs was presented. The model was developed in 2 parts. First, a comprehensive model for rectangular cross-section GAA FETs was derived using the CCDA. It was ensured that the developed model has same mathematical formulation as that of our previous model for cylindrical GAA FETs. Both models were then combined to present a unified model for cylindrical and cuboid geometries. The developed model employed 1D DOS and full Fermi-Dirac statistics, to capture the essential physics of III-V channel with confined geometry. The model was validated by comparing with the data from 2D PS solver for different geometries, dimensions and III-V channel materials and found to be accurate. The model is mathematically simple, analytical, can include higher energy sub-bands without increasing mathematical complexity and is computationally efficient to be used in circuit simulators. The model also includes the structural variations which can occur during the fabrication of GAA FETs, the conduction band non-prabolicity and dimension induced effective mass change.

Appendix 1

According to the CCDA, the $|\Psi_{i,j}(x,y)|^2$ can be approximated, to satisfy the condition of normalization as,

$$\int_{-W/2}^{W/2}\int_{-H/2}^{H/2}|\Psi_{i,j}(x,y)|^2 \mathrm{d}x\mathrm{d}y = 1 \tag{24}$$

Equation (24) is written with the assumption that the entire wavefunction lies within the semiconductor channel. Neglecting the wavefunction penetration in the oxide for the normalization of the wavefunction has little impact on the physics that are more sensitive to the calculation of the quantized energy levels. The finite height of the semiconductor-dielectric barrier is considered in the model via the values of $E_{i,j}$. Since with CCDA, n(x,y) is assumed to be constant within the semiconductor channel, $|\Psi_{i,j}(x,y)|^2$ will also constant.

Evaluating (24) $|\Psi_{i,j}(x,y)|^2$ can be written as,

$$|\Psi_{i,j}(x,y)|^2 = \frac{1}{WH} \tag{25}$$

Appendix 2

Equation (7) with CCDA can be written as,

$$\frac{\partial^2 \Phi(x,y)}{\partial x^2} + \frac{\partial^2 \Phi(x,y)}{\partial y^2} = -\frac{Q_s}{\varepsilon_s WH} \tag{26}$$

Since the source term $-Q_s/\varepsilon_s WH$ is a constant, $\Phi(x,y)$ can be assumed to be of the form $\Phi(x,y) = Ax^2 + By^2 + Cx + Dy + E$. Substituting in (26),

$$A + B = -\frac{Q_s}{2\varepsilon_s WH} \tag{27}$$

The boundary conditions for $\Phi(x,y)$ in a III-V GAA FETs are

$$\left.\frac{\partial \Phi(x,y)}{\partial x}\right|_{x=0} = 0 \tag{28}$$

$$\left.\frac{\partial \Phi(x,y)}{\partial y}\right|_{y=0} = 0 \tag{29}$$

$$\Phi(x,y)\Big|_{x=0,y=0} = \Phi_c \tag{30}$$

Also,

$$\frac{1}{H}\int_{-H/2}^{H/2} \Phi(-W/2,y)\mathrm{d}y = \frac{1}{W}\int_{-W/2}^{W/2} \Phi(x,-H/2)\mathrm{d}x \tag{31}$$

Using the above conditions and analytical solution of $\Phi(x,y)$ can be written as,

$$\Phi(x,y) = -\frac{Q_s}{2\varepsilon_s W^2 + H^2}\left[\frac{H}{W}x^2 + \frac{W}{H}y^2\right] + \Phi_c \tag{32}$$

Appendix 3

The perturbation term can be written as,

$$\Delta Ee_{i,j} = < \Psi^*_{i,j}|\widetilde{\Phi}|\Psi_{i,j} > \tag{33}$$

where the perturbing potential is given by, $\widetilde{\Phi}(x,y) = \Phi(x,y) - \Phi_c$. Here Φ_c is used as the reference to calculate $\mathrm{Eg_{i,j}}$. Using (11) $\widetilde{\Phi}$(x,y) can be written as,

$$\widetilde{\Phi}(x,y) = -\frac{Q_s}{2\varepsilon_s W^2 + H^2}\left[\frac{H}{W}x^2 + \frac{W}{H}y^2\right] \tag{34}$$

Using (34), (33) can be written as,

$$\Delta Ee_{i,j} = -q\int_{-W/2}^{W/2}\int_{-H/2}^{H/2} |\Psi_{i,j}(x,y)|^2\left(-\frac{Q_s}{2\varepsilon_s W^2 + H^2}\left[\frac{H}{W}x^2 + \frac{W}{H}y^2\right]\right)\mathrm{d}x\mathrm{d}y \tag{35}$$

Substituting $|\Psi_{i,j}(x,y)|^2 = 1/WH$ and integrating (35), the perturbation term can be derived as,

$$\Delta Ee_{i,j} = \frac{qQ_s WH}{12\varepsilon_s(W^2 + H^2)} \tag{36}$$

Funding This work is supported by the Visvesvaraya PhD scheme by MeitY, Gover nment of India Enrique G. Marin gratefully acknowledges Juan de la Cierva Incorporation IJCI-2017-32297 (MINECO/AEI).

References

1. Ferain, I., Colinge, C.A., Colinge, J.P.: Multigate transistors as the future of classical metal-oxide-semiconductor field-effect transistors. Nature **479**(7373), 310 (2011). https://doi.org/10.1038/nature10676
2. Kuhn, K.J.: Considerations for ultimate CMOS scaling. IEEE Trans. Electron. Dev. **59**(7), 1813 (2012). https://doi.org/10.1109/TED.2012.2193129
3. Bae, G., Bae, D., Kang, M., Hwang, S.M., Kim, S.S., Seo, B., Kwon, T.Y., Lee, T.J., Moon, C., Choi, Y.M., Oikawa, K., Masuoka, S., Chun, K.Y., Park, S.H., Shin, H.J., Kim, J.C., Bhuwalka, K.K., Kim, D.H., Kim, W.J., Yoo, J., Jeon, H.Y., Yang, M.S., Chung, S., Kim, D., Ham, B.H., Park, K.J., Kim, W.D., Park, S.H., Song, G., Kim, Y.H., Kang, M.S., Hwang, K.H., Park, C., Lee, J., Kim, D., Jung, S., Kang, H.K.: 3nm GAA technology featuring multi-bridge-channel FET for low power and high performance applications. In: IEEE International Electron Devices Meeting (IEDM), pp. 28.7.1–28.7.4. (2018). https://doi.org/10.1109/IEDM.2018.8614629
4. Del Alamo, J.A.: Nanometre-scale electronics with III–V compound semiconductors. Nature **479**(7373), 317 (2011). https://doi.org/10.1038/nature10677
5. Kim, D.H., del Alamo, J.A., Lee, J.H., Seo, K.S.: Performance evaluation of 50 nm $In_{0.7}$ $Ga_{0.3}As$ HEMTs for beyond-CMOS logic applications. In: IEEE International Electron Devices

Meeting, 2005. IEDM Technical Digest, pp. 767–770 (2005). https://doi.org/10.1109/IEDM.2005.1609467
6. Hudait, M.K., Chau, R.: Integrating III–V on silicon for future nanoelectronics. In: 2008 IEEE Compound Semiconductor Integrated Circuits Symposium, pp. 1–2 (2008). https://doi.org/10.1109/CSICS.2008.8
7. Zhao, X., Heidelberger, C., Fitzgerald, E., Lu, W., Vardi, A., del Alamo, J.: Sub-10 nm diameter InGaAs vertical nanowire MOSFETs. In: Electron Devices Meeting (IEDM), 2017 IEEE International, pp. 17.2.1–17.2.4 (2017). https://doi.org/10.1109/IEDM.2017.8268407
8. Ramesh, S., Ivanov, T., Putcha, V., Alian, A., Sibaja-Hernandez, A., Rooyackers, R., Camerotto, E., Milenin, A., Pinna, N., Kazzi, S.E., Veloso, A., Lin, D., Lagrain, P., Favia, P., Collaert, N., Meyer, K.D.: Record performance Top-down $In_{0.53}$ $Ga_{0.47}As$ vertical nanowire FETs and vertical nanosheets. In: 2017 IEEE International Electron Devices Meeting (IEDM), pp. 17.1.1–17.1.4 (2017). https://doi.org/10.1109/IEDM.2017.8268406
9. Kilpi, O.P., Svensson, J., Wu, J., Persson, A.R., Wallenberg, R., Lind, E., Wernersson, L.E.: Vertical InAs/InGaAs heterostructure metal-oxide-semiconductor field-effect transistors on Si. Nano Lett. **17**(10), 6006 (2017). https://doi.org/10.1021/acs.nanolett.7b02251
10. Kilpi, O.P., Svensson, J., Wernersson, L.E.: Sub-100-nm gate-length scaling of vertical InAs/InGaAs nanowire MOSFETs on Si. In: IEEE International Electron Devices Meeting (IEDM), pp. 17–20 (2017). https://doi.org/10.1109/IEDM.2017.8268408
11. Mudanai, S., Roy, A., Kotlyar, R., Rakshit, T., Stettler, M.: Capacitance compact model for ultrathin low-electron-effective-mass materials. IEEE Trans. Electron Dev. **58**(12), 4204 (2011). https://doi.org/10.1109/TED.2011.2168529
12. Yadav, C., Ganeriwala, M.D., Mohapatra, N.R., Agarwal, A., Chauhan, Y.S.: IEEE Trans. Nanotechnol. **16**(4), 703 (2017). https://doi.org/10.1109/TNANO.2017.2709752
13. Ganeriwala, M.D., Ruiz, F.G., Marin, E.G., Mohapatra, N.R.: Compact modeling of gate capacitance in III–V channel quadruple-gate FETs. IEEE Trans. Electron. Dev. **99**, 1 (2018). https://doi.org/10.1109/TED.2018.2866885
14. Dasgupta, A., Agarwal, A., Chauhan, Y.S.: Unified compact model for nanowire transistors including quantum effects and quasi-ballistic transport. IEEE Trans. Electron. Dev. **64**(4), 1837 (2017). https://doi.org/10.1109/TED.2017.2672207
15. Wang, L., Asbeck, P.M., Taur, Y.: Self-consistent 1-D Schrödinger-Poisson solver for III-V heterostructures accounting for conduction band non-parabolicity. Solid-State Electron. **54**(11), 1257 (2010). https://doi.org/10.1063/1.349389
16. Marin, E., Ruiz, F., Tienda-Luna, I., Godoy, A., Sánchez-Moreno, P., Gámiz, F.: Analytic potential and charge model for III–V surrounding gate metal-oxide-semiconductor field-effect transistors. J. Appl. Phys. **112**(8), 084512 (2012). https://doi.org/10.1063/1.4759275
17. Dasgupta, A., Parihar, S.S., Kushwaha, P., Agarwal, H., Kao, M., Salahuddin, S., Chauhan, Y.S., Hu, C.: BSIM compact model of quantum confinement in advanced nanosheet FETs. IEEE Trans. Electron. Dev. **67**(2), 730 (2020). https://doi.org/10.1109/TED.2019.2960269
18. Chakraborty, A.S., Mahapatra, S.: Surface potential equation for low effective mass channel common double-gate MOSFET. IEEE Trans. Electron Dev. **64**(4), 1519 (2017). https://doi.org/10.1109/TED.2017.2661798
19. Numata, T., Uno, S., Hattori, J., Mil'nikov, G., Kamakura, Y., Mori, N., Nakazato, K.: A self-consistent compact model of ballistic nanowire MOSFET with rectangular cross section. IEEE Trans. Electron. Devices **60**(2), 856 (2013). https://doi.org/10.1109/TED.2012.2232928
20. Ruiz, F.J.G., Godoy, A., Gamiz, F., Sampedro, C., Donetti, L.: A comprehensive study of the corner effects in Pi-gate MOSFETs including quantum effects. IEEE Trans. Electron. Dev. **54**(12), 3369 (2007). https://doi.org/10.1109/TED.2007.909206
21. Marin, E.G., Ruiz, F.G., Godoy, A., Tienda-Luna, I.M., Gámiz, F.: Mobility and Capacitance Comparison in Scaled InGaAs Versus Si Trigate MOSFETs. IEEE Electron. Device Lett. **36**(2), 114 (2015). https://doi.org/10.1109/LED.2014.2380434
22. Kim, J., Fischetti, M.V.: Electronic band structure calculations for biaxially strained Si, Ge, and III–V semiconductors. J. Appl. Phys. **108**(1), 013710 (2010). https://doi.org/10.1063/1.3437655
23. Robertson, J., Falabretti, B.: Band offsets of high K gate oxides on III-V semiconductors. J. Appl. Phys. **100**(1), 014111 (2006). https://doi.org/10.1063/1.2213170
24. Ganeriwala, M.D., Yadav, C., Ruiz, F.G., Marin, E.G., Chauhan, Y.S., Mohapatra, N.R.: Modeling of quantum confinement and capacitance in III-V gate-all-around 1-D transistors. IEEE Trans. Electron. Dev. **64**(12), 4889 (2017). https://doi.org/10.1109/TED.2017.2766693
25. Ganeriwala, M.D., Ruiz, F.G., Marin, E.G., Mohapatra, N.R.: A compact model for III–V nanowire electrostatics including band non-parabolicity. J. Comput. Electron. **18**(4), 1229 (2019). https://doi.org/10.1007/s10825-019-01389-1
26. Niquet, Y., Lherbier, A., Quang, N., Fernández-Serra, M., Blase, X., Delerue, C.: Electronic structure of semiconductor nanowires. Phys. Rev. B **73**(16), 165319 (2006). https://doi.org/10.1103/PhysRevB.73.165319